A Computational and Experimental Study of the Cyclic Voltammetry Response of Partially Blocked Electrodes. Part II: Randomly Distributed and Overlapping Blocking Systems

Trevor J. Davies,[†] Benjamin A. Brookes,[†] Adrian C. Fisher,[‡] Kamran Yunus,[‡] Shelley J. Wilkins,[§] Phillip R. Greene,[†] Jay D. Wadhawan,[†] and Richard G. Compton*,[†]

Physical and Theoretical Chemistry Laboratory, Oxford University, South Parks Road, Oxford OX1 3QZ, United Kingdom, Department of Chemistry, University of Bath, Claverton Down, Bath BA2 7AY, United Kingdom, and Department of Materials, Oxford University, Parks Road, Oxford OX1 3PH, United Kingdom

The cyclic voltammetric response of partially blocked electrodes is modeled using finite difference simulations, and a method is presented for the determination of currents at electrode surfaces that have an unstructured blocking pattern. The method is first applied to predict the current at purposely fabricated gold film electrodes in which monodispersed blocking disks are randomly sprinkled over the gold surface. The theoretical models are subsequently applied to the case of a basal plane pyrolytic graphite electrode modified with microdroplets of an electrochemically inactive oil. The theoretically predicted results are in good agreement with those observed experimentally.

1. Introduction

Electrochemical processes at surface-blocked electrodes are interesting to study, not least because the blocking of the transfer of electrons between the electrode and the solution-phase redox species caused by the partial coverage of the electrode surface modifies the absolute and relative rates of diffusive and kinetic fluxes to the electrode but also because of their ubiquity in experiments; although many experiments are plagued by electrode fouling, in some cases (such as those involving electrodes modified chemically,[1] for example, using adsorbates,[2] conducting polymers,[3] or immobilized microparticles[4]), the electrode surface is intentionally blocked. Not surprisingly, significant research has been undertaken for over 30 years to quantify the electrochemistry at partially blocked electrodes (PBEs), primarily to produce a reliable method for interrogating the characteristics of surface blocking.[5−11] Although the large majority of earlier models introduced significant assumptions (such as negligible radial or axial mass transport) or limitations (such as steady-state mass transport), these are only really acceptable for macroscopically inhomogeneous electrode surfaces.[10] The pioneering work by Amatore et al.[10,11] presents a one-dimensional model in which an ensemble of microdisk electrodes are dispersed under a blocking film as a framework for the study of radial diffusion effects induced by the partial blocking of an electrode surface under cyclic voltammetric conditions. In this model, the surface-blocking layer is very small compared to the total diffusion layer (of thickness δ). The radial diffusion regime (individual diffusion layers at each interface) takes place in a thin layer (of thickness μ) adjacent to the electrode surface only, for which $\mu \ll \delta$. Consequently, nonlinear diffusion occurs under stationary conditions in this layer, and thus, the flux from the bulk solution into the layer equals that at the electrode surface.[10] The primary result of the approximate analytical model is that, provided the fractional coverage (θ) is not too close to unity, the cyclic voltammetric response appears less reversible, namely, identical to that at a clean and naked electrode of the same surface area, albeit with a smaller apparent standard rate constant for electron transfer;[10] as the coverage increases, the electron-transfer process becomes more sluggish. Increasing the coverage further effects a decrease in the current height and a modification of the voltammetric waveshape.[10]

The above theory has attracted much attention in the understanding of a plethora of experimental systems;[11] ref 10 has, at the time of writing, over 100 citations and has been applied most noticeably in the elegant experiments employing nanoporous membrane-modified electrodes undertaken by Dryfe and co-workers.[12] In earlier work,[5] we illustrated how the theoretical approach in ref 10 can be extended and adapted via numerical methods to simulate, in two dimensions, the exact inverse problem, that is, the problem of an electrode modified with microscopically small, electrochemically inert, and non-conducting "blocks". We explored this system for regularly distributed blocking patterns and verified the theoretically predicted results, via comparison with experiments conducted with purpose-fabricated "model" gold film electrodes.[5] Of course, the experimental reality is that partially blocked electrodes, unless especially constructed, *do not* have a regular geometry; the blocks are randomly dispersed. This, compounded with the high probability of *overlapping* blocks, may cause further problems in the theoretical modeling of such systems.

It is the aim of this paper to characterize the general transient response of a PBE for which the blocks are distributed across an electrode surface at random intervals. We build up the simulation model developed in Part I,[5] assuming an array of *monodispersed* blocks and mirroring theory employed for the simulation of electrocrystallization phenomena to account for block overlap.[13] These simulation data are applied to two

* To whom correspondence should be addressed. E-mail: richard.compton@chemistry.oxford.ac.uk. Tel: +44 (0) 1865 275 413. Fax: +44 (0) 1865 275 410.
† Physical and Theoretical Chemistry Laboratory, Oxford University.
‡ University of Bath.
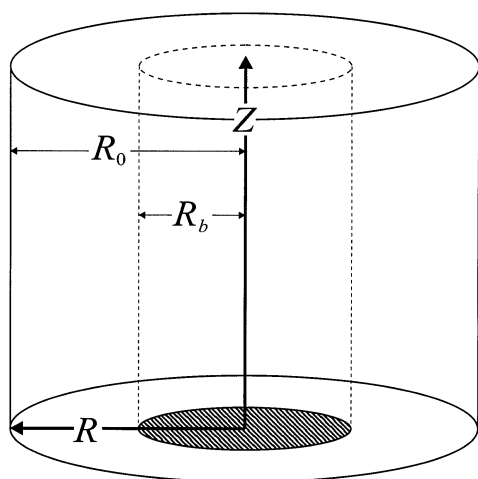§ Department of Materials, Oxford University.

Figure 1. The cylindrical polar coordinate system used to model the blocked electrode surface.

different experimental systems. In the first, as in Part I, we investigate the oxidative voltammetry of *N,N,N′,N′*-tetramethyl-*para*-phenylenediamine (TMPD) in acetonitrile solutions at partially blocked gold-film electrodes, fabricated so as to yield randomly distributed, overlapping blocking insulators. The second experimental system is more challenging in that a basal plane pyrolytic graphite (bppg) electrode surface is modified with microdroplets of *N,N,N′,N′*-tetrahexyl-*para*-phenylenediamine (THPD) via solvent evaporation of an aliquot of solution containing this water-insoluble electroactive oil[14] prior to immersion in aqueous solution so as to study the reductive voltammetry of cobalt(III) sepulchrate trichloride at the exposed graphite electrode. Some of us have pioneered the voltammetry at microdroplet-modified electrodes,[14] and for the case of bppg electrodes modified with microdroplets of THPD, we have shown that the droplets are randomly dispersed with a degree of overlapping microdroplets.[14g] The diameter of the droplets used in typical experiments is on the order of micrometers, the exact size being dependent on the amount of material deposited.[14g] We have further employed such electrodes[15] to mimic electron-transfer processes that take place at electrodes immersed in acoustically emulsified media.[16] Given the utility of such modified electrodes, the simulation of electron-transfer processes at the randomly disordered liquid-modified electrode will have significance in a variety of applications.

2. Theory

The model developed for uniformly distributed blocking systems[5] in Part I is adapted in this section to (i) include the effects of a randomly distributed blocking system and (ii) identify explicitly the role played by blocking disk overlap. To this end, three models (models A, B_1, and B_2) are developed in which the assumption of monodispersed blocking disks or microdroplets prevails. We first, however, briefly recapitulate on the computational method detailed in Part I.

2.1. A Summary of the Model.[5] In Part I, we introduced a method to ascertain the cyclic voltammetric characteristics of a single diffusion domain, a circular inert disk of radius R_b situated at the bottom of a cylinder of radius R_0 (see Figure 1) for the simple redox couple

$$A \underset{k_b}{\overset{k_f}{\rightleftharpoons}} B + e^-$$
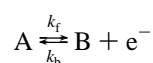
In particular, we developed a protocol that allowed the calcula-

tion of the dimensionless peak current, ψ_{max}, from knowledge of the dimensionless scan rate, ν_{dl}, microscopic coverage, θ, and dimensionless rate constant, k_{dl}^0:

$$\psi_{max} = f(\nu_{dl}, \theta, k_{dl}^0) \tag{1}$$

The three variables in eq 1 are given by

$$\nu_{dl} = \frac{nFR_0^2}{DRT}\nu \tag{2}$$

$$\theta = \left(\frac{R_b}{R_0}\right)^2 \tag{3}$$

$$k_{dl}^0 = \frac{k^0 R_0}{D} \tag{4}$$

where n is the number of electrons transferred at the electrode surface, F is the Faraday constant, ν is the scan rate, D is the diffusion coefficient of the electroactive species, R is the molar gas constant, and k^0 is the heterogeneous rate constant for the redox reaction. By comparison with experimental data obtained for model electrodes, we showed that partially blocked electrodes of high symmetry could be modeled as an ensemble of independent diffusion domains. We now build upon this work by introducing a random nature in the arrangement of the electrochemically inactive, nonconducting disks.

Analytical theory for ensembles of microelectrodes shows that the current is significantly reduced if the distribution of microelectrodes is random as compared to when the microelectrodes are regularly packed.[17] In the case of the microdroplet-modified electrodes, such random microdroplet distribution (which is suggested by imaging of the electrode surface)[14a,14g] would lead to a significant variation in the mean center-to-center microdroplet distance and hence the value of both θ and R_0 in the diffusion domains. Because the current is a distinctly nonlinear function of the parameters θ and R_0, it is essential that we attempt to incorporate statistics of the microscopic variation in droplet distribution into the model.

While blocking disk geometry is an important criterion in determining current results, droplet size will also contribute to changes in the dimensionless current. Previous imaging[14g] showed that the spread of radii of the droplets was small, and to simplify our model considerably, we assume that the droplet radii are monodispersed. To rationalize such effects, we analyze the experimental data using the two distinct models for droplet distribution. This will not only illustrate the effects of the role that droplet geometry plays in the predicted current, but later after consideration of electrode surface imaging data, the validity of both models can be assessed. However, we first consider model electrodes fabricated to mimic droplet-modified electrodes, that is, a polydisperse set of diffusion domains of a monodisperse set of inert disks.

2.2. Modeling a Random Distribution of Inert Disks. Figure 2 illustrates a random array of blocks of radius 100 μm on a square electrode of length 5 mm. The global coverage, Θ, is defined as

$$\Theta = \frac{N_{block}\pi R_b^2}{A_{elec}} \tag{5}$$

where N_{block} is the number of disks on the electrode surface of total area A_{elec}. In the case of Figure 2, $N_{block} = 79$ and $\Theta = 0.1$. The global coverage is actually greater than the true
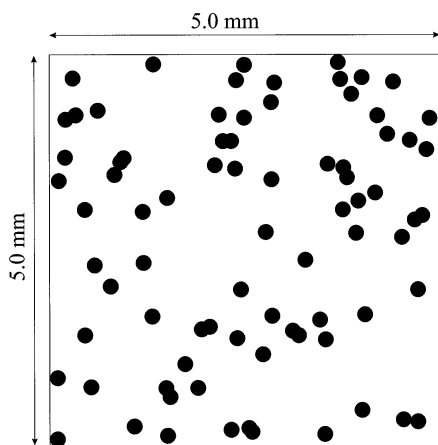
CV Response of Partially Blocked Electrodes. Part II

J. Phys. Chem. B, Vol. 107, No. 26, 2003 **6433**

Figure 2. Template of a random distribution of inert disks on a 5 mm × 5 mm electrode surface where $R_b = 100\ \mu$m, $\Theta = 0.1$, and $N_{block} = 79$.

coverage, Θ_R, because of the overlap of disks. Images similar to Figure 2 were used as templates in the fabrication of the model electrodes.

For the purpose of the model, we assume that the blocked surface is comprised of inert disks, which contact the electrode surface through a circular base of surface radius, R_b. If the block distribution is random (there is no correlation between neighboring blocks), there will be no ordering in their geometrical layout on the electrode surface. Associated with each blocking disk (i) is a diffusion area, A_i, such that $\sum_i A_i = A_{elec}$. We approximate each of these diffusion areas as circular domains. Thus, as in Part I,[5] we can consider the blocked electrode surface as an ensemble of independently interacting cylindrical units,[18] the only difference being the relationship between R_b and R_0 (vide infra). The aim of the models proposed below is to predict a value of R_b for a fabricated model random electrode of known Θ and constant R_b (monodispersed block radii).

2.2.1. Model A: Monodisperse Distribution of Diffusion Domains. It is assumed that all blocks are regularly dispersed on the surface of the electrode without specifying the geometry of the packing, that is, R_0 is constant. The circle enclosed by half the average nearest-neighbor distance around any block determines the amount of electrode area occupied by each block. The summation of all diffusional domain areas corresponds to the total electrode area, A_{elec}:

$$A_{elec} = N_{block} \pi R_0{}^2 \qquad (6)$$

Comparison of eqs 5 and 6 yields the relationship between R_0 and R_b:

$$R_0 = R_b / \sqrt{\Theta}$$

where the global coverage, Θ, is known. Because inert blocking disks are regularly distributed, in the limit $\theta \to 1$, no disk overlap occurs. The fact that each diffusion domain is identical means that the (peak) dimensionless current for the whole electrode will be equal to that for a single domain ($\theta = \Theta$).

To calculate the predicted block radius, R_b^{opt}, we specify a range of values of the droplet radius, R_b. Using the global coverage, Θ, we may calculate the diffusion domain radius, R_0. This allows the determination of the dimensionless scan rate, ν_{dl}, and the homogeneous rate constant, k_{dl}^0 (the microscopic coverage, θ, equals the global coverage, Θ). Thus, from eq 1, we have sufficient information to predict the dimensionless peak

current for the particular domain and, therefore, the total electrode dimensionless peak current, ψ_{max}. The relationship between the peak (nondimensionless) current, I_p, and ψ_{max} is given by

$$I_p = [A]_{bulk} A_{elec} \sqrt{\frac{F^3 D \nu}{RT}} \psi_{max} \qquad (7)$$

in which $[A]_{bulk}$ is the bulk concentration of the electroactive species A, and the other symbols have been defined earlier. The value of R_b for which the difference between experimental and theoretical dimensionless current is minimized is denoted R_b^{opt}.

2.2.2. Model B: Polydisperse Distribution of Diffusion Domains. We assume that all inert disks on the electrode surface have the same radius, R_b, but are distributed in a random nature. Hence, there will be a range of diffusion domains of different sizes, R_0. Equations are available for the statistical treatment of nearest-neighbor distance in a random distribution of particles.[19] For particles of infinitesimal size suspended on an infinite two-dimensional surface, the probability that two nearest neighbors will occur with a separation x is given by

$$P(x) = 2\pi x n\, e^{-\pi x^2 n} \qquad (8)$$

where n is the particle density (the number of particles divided by the area of the surface, which in our case is N_{block}/A_{elec}).[19,20] The expectation for the nearest-neighbor separation is therefore $\langle x \rangle = (4n)^{-1/2}$. Our dimensionless peak current prediction requires information about the unblocked electrode area encircled by each droplet to calculate the microscopic coverage, θ. Clearly by geometric observation, setting R_0 equal to $x/2$ cannot be correct because unaccounted electrode area will always be left between blocking disks. If R_0 is set equal to x, the average size of the diffusion domain areas, $E(\pi x^2)$, is given by eq 9.

$$E(\pi x^2) = \int_0^\infty P(x)\pi x^2\, dx = 1/n = A_{elec}/N_{block} \qquad (9)$$

Hence, $A_{elec} = N_{block} E(\pi x^2)$, and the expectation value of the diffusional domain area is equal to the average electrode area around a single insulating disk.

In a similar procedure to that used in model A, we calculate the global peak dimensionless current, ψ_{max}, for a range of R_b values. Consider an arbitrary domain of radius r_0 and block radius r_b. Equation 1 allows us to calculate ψ_{max} for this domain, which we denote $\psi_{max}^{r_b}(r_0)$. Using the global coverage, Θ, and the electrode area, A_{elec}, we can calculate the number of blocks, N_{block} (eq 5), and the block density, n, for our particular block radius. The probability that a domain with radius $r_0 + \delta r_0$ occurs is then given by $P(r_0)\delta r_0$. Multiplying by N_{block} returns the number of domains of this size that are on our model electrode surface. With the use of eq 7, the contribution of this particular domain to the total (nondimensionless) current, $I_p^{r_b}(r_0)$, is given by

$$I_p^{r_b}(r_0) = [A]_{bulk} A_{elec} \sqrt{\frac{F^3 D \nu}{RT}} \psi_{max}^{r_b}(r_0) =$$

$$[A]_{bulk}[N_{block} \pi r_0{}^2 P(r_0)\delta r_0] \sqrt{\frac{F^3 D \nu}{RT}} \psi_{max}^{r_b}(r_0) \qquad (10)$$

For our particular r_b, we need to calculate the total current, $I_p^{r_b}$, which is the sum of the contributions from every domain size.
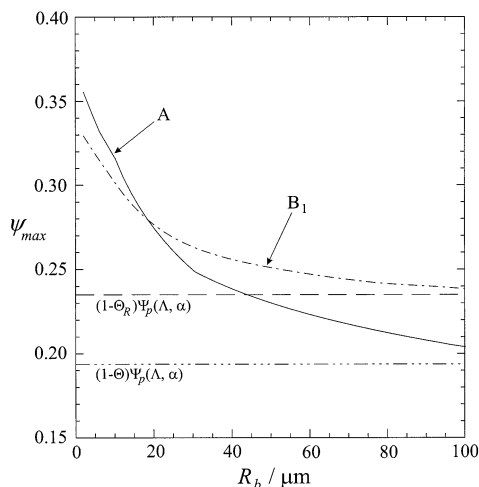
Figure 3. Simulation of the dimensionless peak current response over a range of R_b values according to models A (—) and B_1 (− · −) for a fabricated electrode where $v = 1.0$ V s^{-1}, $A_{elec} = 0.3$ cm^2, $\Theta = 0.5$, $D = 1.9 \times 10^{-5}$ cm^2 s^{-1}, $k_0 = 1.4 \times 10^{-2}$ cm s^{-1}, and $T = 292$ K. The overlaid horizontal lines (dashed) represent the limiting dimensionless currents mentioned in the text.

Therefore, we repeat the above calculation for the full range of R_0 values, noting that θ, v_{dl}, and k_0 are dependent on R_0 whereas N_{block} is not:

$$I'^{r_b}_p = N_{block}\pi[A]_{bulk}\sqrt{\frac{F^3 D v}{RT}}\int_0^\infty R_0{}^2\psi'^{r_b}_{max}(R_0)P(R_0)\,dR_0 \tag{11}$$

The probability of domains with radii greater than $3\langle R_0\rangle$ is so small that their current contribution is negligible and the upper limit of infinity can be replaced by $3\langle R_0\rangle$. Having established the total current for a particular value of block radius, $I'^{r_b}_p$, we convert back to dimensionless current using eq 7:

$$\psi'^{r_b}_{max} = \frac{I'^{r_b}_p}{[A]_{bulk}A_{elec}\sqrt{\dfrac{F^3 D v}{RT}}} =$$

$$\frac{\pi N_{block}}{A_{elec}}\int_0^{3\langle R_0\rangle} R_0{}^2\psi'^{r_b}_{max}(R_0)P(R_0)\,dR_0 \tag{12}$$

As in model A, the theoretically predicted value of the block radius, R_b^{opt}, is the block radius for which the difference between experimental and theoretical current is minimized.

A hidden feature of this model is that it actually takes the overlap of blocks into account. Consider situations in the calculation above where $r_0 < r_b$. In our model, these domains have a finite probability of occurring and correspond to the overlapping of droplets. Because $\theta > 1$ for the case $r_b > r_0$, these domains are assigned a $\psi'^{r_b}_{max}(r_0)$ value of zero in the calculation. Therefore, regardless of whether we start the integration in eq 12 at zero or r_b, we obtain the same result for the total dimensionless current, $\psi'^{r_b}_{max}$, because between zero and r_b we only consider domains where $\psi'^{r_b}_{max}(R_0) = 0$. It is in this way that the model, which we denote "model B_1", accounts for overlap. We apply the same ideas to the problem of inert microdroplets on an electrode surface in section 2.3. We first compare the theoretical predictions of model A and B_1.

2.2.3. Simulation Results for Randomly Distributed Blocking Disks: Models A and B_1. Figure 3 illustrates a simulation of
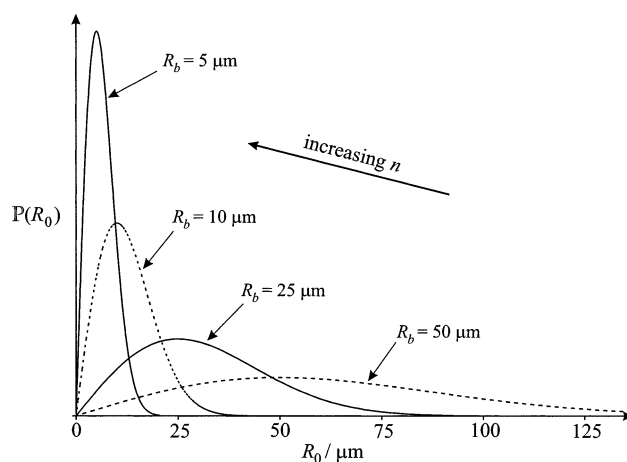

Figure 4. The probability function in eq 8 for differing values of n, where $\Theta = 0.5$ and the different values of R_b are given in the figure.

models A and B_1 in which ψ_{max} is plotted against R_b for a system in which $A_{elec} = 0.3$ cm^2, $D = 1.9 \times 10^{-5}$ cm^2 s^{-1}, $k_0 = 1.4 \times 10^{-2}$ cm s^{-1}, $v = 1.0$ V s^{-1}, and $\Theta = 0.5$. Although the unblocked electrode area is constant, in both models, we observe a decrease in ψ_{max} with increasing R_b. This can be explained by considering the singularities that occur at the block-electrode boundary, that is, the point at which the flux of electroactive species to the surface is infinite. Logically, the more of these points, the higher the overall (dimensionless) current should be. The perimeter, l, of a block is an indication of how many singularities there are and is given by

$$l = 2\pi R_b \tag{13}$$

Thus, the total perimeter of all of the blocks, l_{tot}, is given by

$$l_{tot} = 2N_{block}\pi R_b = \frac{2\Theta A_{elec}}{R_b} \tag{14}$$

Therefore, as R_b increases, l_{tot} decreases, and we have fewer points of singularity resulting in smaller values of ψ_{max}.

The two models "cross over" because of two limiting factors. As R_b increases, R_0 increases (in both models) resulting in an increase in the dimensionless scan rate, v_{dl}. As shown earlier,[5] in the limit $v_{dl} \rightarrow \infty$, the dimensionless peak current, ψ_{max}, approaches $(1 - \Theta_R)\Psi_p(\Lambda,\alpha)$, where $\Psi_p(\Lambda,\alpha)$ is the dimensionless peak current predicted by linear diffusion theory (i.e., that for an unblocked electrode) in which $\Lambda = k_{dl}^0/v_{dl}$ and α is the charge-transfer coefficient. Because of disk overlap, Θ_R is smaller than Θ, meaning $(1 - \Theta_R)\Psi_p(\Lambda,\alpha)$ is greater than $(1 - \Theta)\Psi_p(\Lambda,\alpha)$. The latter two values are overlaid in Figure 3. We can see that model A, in which we assume that the disks do not overlap, approaches $(1 - \Theta)\Psi_p(\Lambda,\alpha)$ as v_{dl} increases (R_b increases), whereas model B_1, in which block overlap is accounted, approaches the true dimensionless peak current limit, $(1 - \Theta_R)\Psi_p(\Lambda,\alpha)$. Thus at high scan rates, we observe a breakdown in model A.

At low values of R_b, model A predicts a greater ψ_{max} than model B_1. This is due to the probability function used in model B_1 (eq 8 where $R_0 = x$), which is illustrated in Figure 4. As the particle density, n, increases, the spread of R_0 diminishes and becomes more concentrated around the peak value, R_0(peak), given by the value of R_0 that satisfies

$$\frac{d}{dR_0}(2\pi R_0 n\, e^{-\pi R_0{}^2 n}) = 0 \tag{15}$$

CV Response of Partially Blocked Electrodes. Part II

J. Phys. Chem. B, Vol. 107, No. 26, 2003 **6435**

The solution of eq 15 yields

$$R_0(\text{peak}) = \frac{1}{\sqrt{2\pi n}} = \frac{R_b}{\sqrt{2\Theta}} \qquad (16)$$

In the limit $n \to \infty$, R_0 simply becomes $R_0(\text{peak})$. At low values of R_b, the block density is large, and we have a situation in which $R_0 \approx R_0(\text{peak})$, that is, the range of probable R_0 values is tiny and centered around $R_0(\text{peak})$. However, the value of R_0 in model A is constant and equal to $R_b/\sqrt{\Theta}$, which is $2^{1/2}$ times greater than R_0 for model B_1. Thus at low values of R_b, model A has a lower θ than model B_1 resulting in larger values of ψ_{max}.

2.3 Modeling a Random Distribution of Inert Hemispheres/ Microdroplets. We assume that each droplet is hemispherical in geometry and, therefore, contacts the electrode surface through a circular base of surface radius R_b. As in the previous models, the diffusion around each droplet is symmetric in the radial direction. The volume of blocking material, V_{block}, is given by the equation

$$V_{\text{block}} = \frac{2}{3}N_{\text{block}}\pi R_b{}^3 \qquad (17)$$

where N_{block} is the number of droplet hemispheres/blocks. Notice that a major assumption of eq 17 is that if the droplets overlap they must retain their circular base. The global coverage, Θ, is the same as in the previous models and is given by eq 5.

Our protocol for calculating the dimensionless current for a particular diffusion domain (eq 1) does so for a flush surface. However, microdroplets are three-dimensional and extend above the surface of the electrode. Therefore, in extending the above models we must either neglect the diffusional perturbation that results from the height of the droplet or modify our original problem in Part I. To the authors' knowledge no research on PBEs has included raised or recessed blocking effects, and because the inclusion of sessile droplet geometry to define diffusional boundary conditions would result in the loss of model generality, we have chosen to ignore it. Moreover, the exact microdroplet geometry depends on the contact angle at the three-phase boundary, which varies on many physical parameters, such as electrode material, solvent viscosity, and liquid|liquid surface tension effects, all of which may cause the microdroplets to be lenticular.[21] In the following sections, we thus assume that the monodispersed microdroplets approximate as inert disks, that is, the radial protrusion of the droplets from the electrode surface is negligible compared with the diffusion layer. Furthermore, because the height of the blocking sites is not a parameter in this work, provided this remains small compared with the interdroplet distance, the shape of the blocking site above the electrode plane is not very relevant.

2.3.1. Model A: Monodisperse Distribution of Diffusion Domains. As in the previous model A, we assume that all droplets are regularly dispersed on the surface of the electrode, that is, every diffusion domain is identical. Consequently, R_0 is constant for a certain value of R_b, and the dimensionless peak current, ψ_{max}, for one diffusion domain will be equal to that for the whole electrode ($\Theta = \theta$). Note that this model assumes that no droplet overlap occurs in the range $0 < \theta < 1$. We need to calculate a value of R_0 for a particular value of R_b, and as before, we can use $R_0 = R_b/\sqrt{\Theta}$ where the global coverage, Θ, is given by eq 5. However, in the case of microdroplets on an electrode surface, we have no prior knowledge of Θ or N_{block}, so we have an equation with two unknowns. Thus, rearranging eq 17 to obtain an expression for N_{block}, we may use eq 5 to

obtain an expression for Θ. The resulting equations contain just one unknown each (V_{block} is measured experimentally, and we have assumed a value for R_b):

$$N_{\text{block}} = \frac{3V_{\text{block}}}{2\pi R_b{}^3} \qquad (18)$$

$$\Theta = \frac{3V_{\text{block}}}{2R_b A_{\text{elec}}} \qquad (19)$$

For a certain volume of blocking material, using eq 19 with the relationship $R_0 = R_b/\sqrt{\Theta}$ allows us to calculate values of θ, ν_{dl}, and k_{dl}^0 for a given R_b. Hence, we have sufficient information to calculate ψ_{max} for a range of R_b values assuming V_{block} is known.

2.3.2. Model B: Polydisperse Distribution of Diffusion Domains. To extend the previous model B_1 to include micro-droplets, we simply replace the disks with "flat" hemispheres. To avoid overcomplication, we assume that when the droplets overlap, their geometry at the surface does not change (i.e., overlapping droplets keep their circular base), whereas their shape above the surface is undefined. This questionable assumption allows us to use eq 5 to calculate the global coverage, Θ, and we shall discuss its validity later. Thus, we can use eq 12 to calculate ψ_{max} for a range of R_b values, the only modification being in the calculation of N_{block} (and, therefore, n), which is accomplished using eq 18.

However, the new model B_1 predicts *the radii of the overlapping droplets*, which is not the same as *the radii of the droplets formed from overlap* (i.e., the droplets as seen through a microscope). That is, model B_1 predicts a limiting size of microdroplet, the size expected were there no overlap. Thus, if the approximations of the model are viable, it should predict a constant R_b value, no matter what the coverage. For example, even in a situation in which there is much droplet overlap, model B_1 will predict the size of the droplet that makes up the bigger droplets. We therefore need to adjust the model so that it predicts the droplet size that would be "seen through a microscope" rather than the "building-block" size. The simplest way to do this is to replace each R_b value in model B_1 with a real average droplet radius, $R_b{}'$.

We next propose a different model, model B_2. Theory has been developed by Evans[20] and Avrami[22] for the prediction of global coverage, Θ, when there is significant droplet overlap: if centers of growth are nucleated randomly on a surface and growth initiated at an identical point in time, the true coverage of the surface, Θ_R, assuming each droplet grows evenly in every direction, is given by

$$\Theta_R = 1 - e^{-\Theta} \qquad (20)$$

In model B_2, we approximate the overlapped droplets of model B_1 as *larger droplets that do not overlap*. These larger droplets have a surface radius of $R_b{}'$. Thus, $R_b{}'$ is related to the real coverage, Θ_R, in exactly the same way that R_b is related to Θ:

$$\Theta_R = \frac{N_{\text{block}}{}'\pi(R_b{}')^2}{A_{\text{elec}}} = \frac{3V_{\text{block}}}{2A_{\text{elec}}R_b{}'} \qquad (21)$$

For each value of R_b (the "building-block" radius), we can calculate an average radius that accounts for overlapping, $R_b{}'$, using eq 21. We then plot this value of $R_b{}'$ against our dimensionless peak current calculated from model B_1, ψ_{max}-(R_b). Because Θ_R is always less than Θ, $R_b{}'$ is always larger
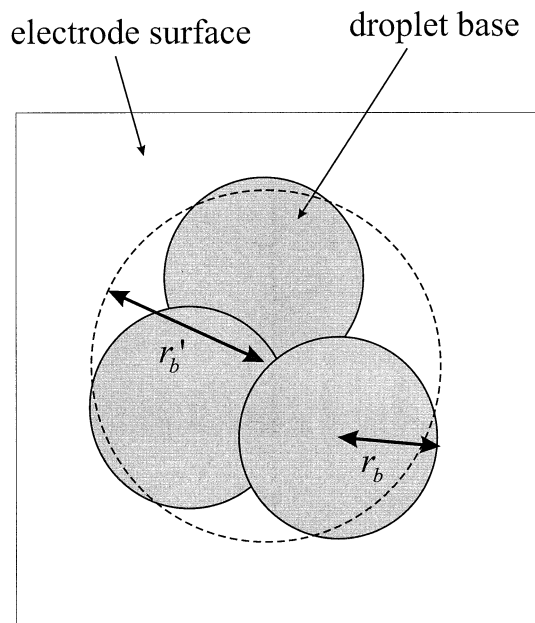
Figure 5. The difference between r_b and r_b': an arbitrary situation in which three droplets of radius r_b overlap (according to the assumption of model B). The resulting droplet can be approximated as a larger droplet of radius r_b'. Only the circular bases are shown because the geometry above overlapping droplets is undefined in model B_1.

than R_b, as expected. Also, in the limit of $V_{block} \rightarrow 0$ ($\Theta \rightarrow 0$), $R_b' \rightarrow R_b$ and the two models B_1 and B_2 should be identical.

Figure 5 illustrates an arbitrary situation in which we have three droplets, of radius r_b, on an electrode surface that overlap to give a larger droplet, of approximate radius r_b'. In both models, the dimensionless peak current for this electrode is $\psi_{max}(r_b)$. In model B_1, $\psi_{max}(r_b)$ is associated with the radius r_b, whereas in model B_2, $\psi_{max}(r_b)$ is associated with r_b'. Thus, the difference between the two models is subtle, and the simulation of model B_2 becomes simple once the calculations for B_1 have been completed.

As an aside, consider the total area over which ψ_{max} is calculated, A. This can be written as follows:

$$A = \int_0^\infty N_{block} \pi (R_0^2 - R_b^2) P(R_0) \, dR_0 =$$

$$\frac{2\pi^2 N_{block}^2}{A_{elec}} \int_0^\infty R_0 (R_0^2 - R_b^2) \, e^{-\pi R_0^2 N_{block}/A_{elec}} \, dR_0 \quad (22)$$

where

$$\int_0^\infty x \, e^{-ax^2} \, dx = \frac{1}{2a}$$

and

$$\int_0^\infty x^3 \, e^{-ax^2} \, dx = \frac{1}{2a^2}$$

Thus, we obtain

$$A = A_{elec}(1 - \Theta) \quad (23)$$

However, if we change the lower limit in eq 22 to R_b, because ψ_{max} is only calculated in the region $R_b < R_0 < \infty$, and use the substitution $s = \pi R_0^2 N_{block}/A_{elec}$, we obtain

$$A = A_{elec} e^{-\Theta} = A_{elec}(1 - \Theta_R) \quad (24)$$

This is the true unblocked area of the electrode and shows how model B takes into account block/droplet overlap.

2.3.3. Simulation Results for Microdroplet-Modified Electrodes. Figure 6a−f illustrates the dependence of the dimensionless peak current, ψ_{max}, on the droplet size, R_b, for models A, B_1, and B_2 over a range of six blocking volumes at a scan rate of 0.05 V s^{-1}. The effect of taking overlap into account is apparent in the differences between models A and B (B_1 and B_2). As R_b increases, there is a decrease in both Θ and N_{block} (and therefore n). Thus the spread of probable R_0 values in models B_1 and B_2 increases (as well as $\langle R_0 \rangle$), and we observe a gentle increase to the limiting value of ψ_{max}. In the case of model A, however, we observe a rapid increase to this limiting value due to there being only one R_0 value for each R_b.

At large values of R_b, models A and B converge to one limiting peak dimensionless current, whereas in section 2.2.3, they converged to two different limits. In the case of microdroplets, for a constant block volume, as R_b increases the corresponding decrease in Θ is fairly rapid. Thus, at large values of R_b (where $\nu_{dl} \rightarrow \infty$), the difference between Θ and Θ_R is negligible, so both models tend to the same limit: $(1 - \Theta_R) \times \Psi_p(\Lambda, \alpha) \approx (1 - \Theta) \Psi_p(\Lambda, \alpha)$.

In the limit $V_{block} \rightarrow 0$ and $R_b \rightarrow R_b(max)$ (where $R_b(max)$ is the radius of a droplet of volume V_{block}) we encounter situations in which Θ approaches 0. At low values of Θ, $1 - e^{-\Theta} \approx \Theta$ and $\Theta_R \approx \Theta$. Thus in both of these limits, we observe the merging of models B_1 and B_2. In other words, at low coverage, there is little droplet overlap and $R_b' \approx R_b$.

One final observation from Figure 6 is the difference in where $\psi_{max} = 0$ between models A_1 and B_2 and model B_1. Both models A and B_2 give the predicted current for an electrode surface of *nonoverlapping* droplets. Therefore, the maximum value of R_b for which $\psi_{max} = 0$, $R_b(min)$, will correspond to $\Theta = 1$ in eq 19 (in the case of model A) or $\Theta_R = 1$ in eq 21 (model B_2). Both of these conditions give the following relationship:

$$\psi_{max} = 0; \quad R_b(min) = \frac{3V_{block}}{2A_{elec}} \quad (25)$$

Thus, both models A and B_2 have the same $R_b(min)$ value, which is marked on the relevant figures (black circles). In the case of model B_1, we deal directly with overlapping droplets and $\psi_{max} \rightarrow 0$ as $\Theta_R \rightarrow 1$. From eq 20, this requires that $\Theta \rightarrow \infty$ and hence $R_b \rightarrow 0$. Therefore, model B_1 should always have $R_b(min) = 0$. At high block volumes in Figure 6, model B_1 appears to have $R_b(min)$ values slightly greater than zero, which is due to our electrode surface not being an infinite two-dimensional plane.

We next apply these theoretical models to experimental systems so as to deduce the most "realistic" case.

3. Experimental Section

3.1. Chemical Reagents. *N*,*N*,*N′*,*N′*-Tetrahexyl-*para*-phenylenediamine (THPD) was synthesized following a literature procedure.[14] Electrolyte reagents, sodium perchlorate, octaazabicyclo[6.6.6]eicosane cobalt(III) trichloride (subsequently referred to as cobalt(III) sepulchrate trichloride), and *N*,*N*,*N′*,*N′*-tetramethyl-*para*-phenylenediamine (TMPD), all from Aldrich, and tetrabutylammonium perchlorate (TBAP, Fluka, electrochemical grade) were purchased in the purest commercially available grade. Water with a resistivity of not less than 18 MΩ cm used to make the electrolyte solutions was taken from an Elgastat system (USF, Bucks, U.K.). Dried and distilled acetonitrile used to make nonaqueous solutions was purchased from Fisons and used
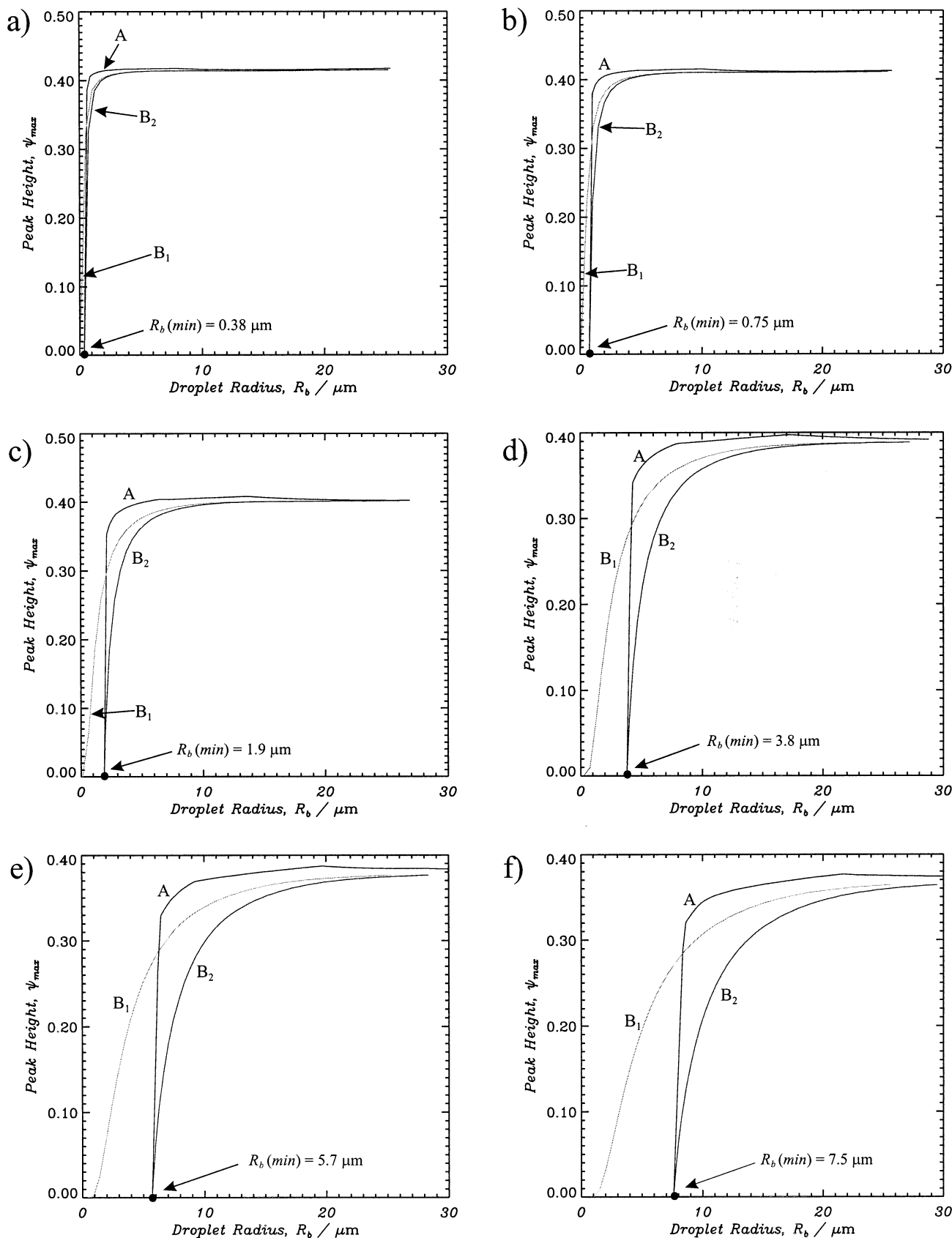
CV Response of Partially Blocked Electrodes. Part II

J. Phys. Chem. B, Vol. 107, No. 26, 2003 **6437**

Figure 6. Simulation of the dimensionless peak current response over a range of R_b values according to models A, B_1, and B_2 for a microdroplet partially blocked electrode. In all six cases, $v = 0.05$ V s^{-1}, $D = 6.7 \times 10^{-6}$ cm^2 s^{-1}, $k_0 = 7.0 \times 10^{-3}$ cm s^{-1}, $A_{elec} = 0.19$ cm^2, and $T = 298$ K. The volume of blocking material on the electrode surface is (a) 4.77×10^{-6}, (b) 9.55×10^{-6}, (c) 2.39×10^{-5}, (d) 4.77×10^{-5}, (e) 7.16×10^{-5}, and (f) 9.55×10^{-5} cm^3. These volumes correspond to amounts of 10, 20, 50, 100, 150, and 200 nmol when the density and relative molecular mass of the blocking material are 0.93 g cm^{-3} and 444 g mol^{-1}, respectively (as for the case of THPD).

without further purification. All solutions and materials were outgassed with oxygen-free nitrogen (BOC Gases, Guildford, Surrey, U.K.) prior to experimentation. All experiments were conducted at 20 ± 2 °C.
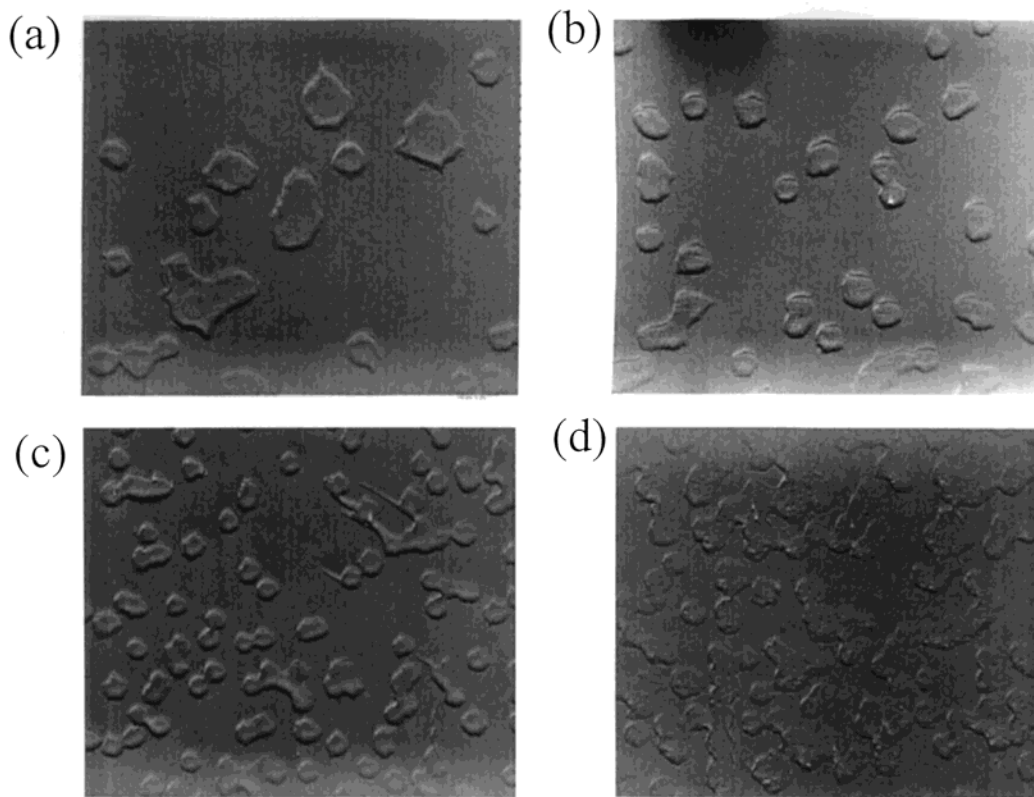
Figure 7. SEM images of the partially blocked gold film electrodes especially constructed for this work with fractional coverage $\theta =$ (a) 0.05, (b) 0.15, (c) 0.25, and (d) 0.5. The blocking disks are sprinkled over the gold film surface.

3.2. Instrumentation. Electrochemical experiments were undertaken in a conventional three-electrode cell, employing a working electrode (vide infra), a gold wire counter electrode, and a reference electrode. In aqueous solutions, a saturated calomel reference electrode (SCE, Radiometer, Copenhagen, Denmark) was used; in nonaqueous solutions, this electrode was replaced by a silver wire pseudo-reference. For nonaqueous experiments, a 5.0×5.0 mm^2 partially blocked gold film working electrode was used with a 5.5 mm diameter gold disk electrode providing a fully unblocked surface. This latter electrode was polished using a 1.0 μm alumina slurry (Beuhler, Lake Bluff, IL) and rinsed in water and acetonitrile prior to deployment. For experiments conducted in aqueous solutions, a 4.9 mm diameter basal plane pyrolytic graphite electrode (bppg, Le Carbone, Ltd., Sussex, U.K.) was employed as the working electrode. Electrochemical data were recorded using either an Oxford Electrodes analogue potentiostat (Oxford, England) connected to a Lloyd PL3 chart recorder (JJ Instruments, Southampton, U.K.) or a commercially available computer-controlled potentiostat (AUTOLAB PGSTAT30, Eco-Chemie, Utrecht, The Netherlands).

The bppg working electrode was modified with microdroplets of THPD by solvent evaporation of an aliquot of ca. 1−10 mM THPD/MeCN stock solution (accurately known). Oxygen dissolved in the THPD microdroplets was removed by degassing using nitrogen: the modified electrode was placed in a slow stream of nitrogen for at least 15 min prior to immersing the electrode in the aqueous electrolyte. The electrode was cleaned immediately prior to experimentation by rinsing with acetonitrile and water, and the surface was renewed by polishing on carborundum paper (P1000 grade, Acton and Bormans, Stevenage, U.K.).

The gold film partially blocked electrodes were prepared and used following procedures previously outlined.[5] Eight electrodes, each corresponding to a known fractional coverage, 0.05, 0.15, 0.25, and 0.5, were fabricated with insulating blocking disks of radii 25, 40, 50, and 75 μm, respectively. The blocking sites in these electrodes were randomly distributed, and as previously,[5] the electrodes were fabricated from computer-generated templates using a random number generator to specify the Cartesian coordinates of the blocking disks.

Both types of partially blocked electrodes were visually inspected so as to confirm the size and distribution of the electrodes. The gold film partially blocked electrodes were imaged using scanning electron microscopy (SEM) achieved using a Hitachi s520. THPD microdroplets immobilized on a freshly cleaved bppg fragment were viewed directly using a Leica DMLM microscope. A 10× Leica C Plan achromat objective with numerical aperture of 0.22 was used without a cover slip. The microscope was coupled to a YC-05 image sensor video camera, and the image was saved digitally.

3.3. Computation. All computational protocols used have been reported in Part I of this series, to which the interested reader is directed.[5] To model the microdroplet-modified electrode, the integral in eq 12 was divided into 100 intervals for both models B$_1$ and B$_2$ and further analysis was undertaken using IDL 5.0.

4. Experimental Results and Discussion

The electrochemistry of two different redox systems was investigated using the partially blocked electrodes. With gold-film PBEs, the oxidation of TMPD in acetonitrile solution was interrogated; in contrast, because the THPD-modified electrode can be electrochemically oxidized to yield the THPD$^{+\bullet}$ cation radical at potentials greater than 0 V vs SCE,[14] we sought to interrogate the redox activity of a species that is *reduced* at potentials negative of 0 V vs SCE. Thus, at the THPD

CV Response of Partially Blocked Electrodes. Part II

J. Phys. Chem. B, Vol. 107, No. 26, 2003 **6439**

microdroplet-modified electrode, the electrochemical reduction of cobalt(III) sepulchrate trichloride in aqueous solution was studied.

4.1. Partially Blocked Gold Film Electrodes. *4.1.1. Visual Inspection of the Electrodes.* Figure 7 presents images of all of the 5 × 5 mm square partially blocked electrodes employed in this work. The randomness of the distribution is readily apparent. Clusters, formed by an agglomeration of blocking disks, evidence the occurrence of blocking disk overlap. Although the large majority of the blocking disks look good, imperfections in the fabrication of these model electrodes, such as noncircular blocks (see Figure 7a) or porous blocks (see Figure 7d), are nevertheless present. These faults will influence the observed voltammetry; we will treat minor deviations as "experimental error".

4.1.2. Experiment vs Theory. To determine the diffusion coefficient, D, and heterogeneous rate constant, k_0, for TMPD oxidation in 0.1 M TBAP/MeCN, cyclic voltammetry experiments were performed using a 5.5 mm diameter unblocked gold electrode. Analysis of the peak currents using the Randles−Sevčik equation and the peak-to-peak separation data using Nicholson's treatment[23] yielded values of $D = (1.9 \pm 0.2) \times 10^{-5}$ cm^2 s^{-1} and $k_0 = (1.4 \pm 0.2) \times 10^{-2}$ cm s^{-1}, in good agreement with literature values.[5] Cyclic voltammetric experiments were then undertaken on all four of the fabricated electrodes ($\Theta = 0.05, 0.15, 0.25,$ and 0.5) using six scan rates in the range $0.02 \leq \nu \leq 1.0$ V s^{-1}. The simulations described in section 2.2.3, in which ψ_{max} is calculated for a range of R_b, were performed for each of the four Θ values at each scan rate for both models A and B$_1$. Figure 8a,b shows the results of the $\Theta = 0.5$ simulation with the experimentally observed results overlaid (transformed into dimensionless form using eq 7). The line labeled "error" is given by the equation

$$\text{error}(R_b) \propto \sum_{i=1}^{6} (\psi_{max}^i(R_b) - \psi_{max}^i(\text{exptl}))^2 \qquad (26)$$

where $\psi_{max}^i(R_b)$ is the value of ψ_{max} at the block radius R_b for a scan rate i, $\psi_{max}^i(\text{exptl})$ is the experimental value of ψ_{max} at the scan rate i, and $i = 1, 2, 3, 4, 5,$ and 6 represents the six scan rates $\nu = 0.02, 0.05, 0.1, 0.2, 0.5,$ and 1.0 V s^{-1}, respectively. The predicted block radius, R_b^{opt}, is thus the value of R_b for which the error is a minimum. Table 1 displays the "actual" and theoretically predicted block radii, R_b^{opt}, for both models. Figure 9a−d illustrates the variance of the experimental, predicted, and unblocked current with the square root of the scan rate, in which the value of R_b used in the calculation for the predicted current is the "actual" R_b value shown in Table 1. Comparing the data in Table 1, we see that both models A and B$_1$ are in good agreement with the experimental data, most disagreement being for the lowest coverage, $\Theta = 0.05$. As noted in Part I, the models cannot be expected to work well for electrodes of low coverage because of the tiny variation of ψ_{max} with R_b.[5]

As noted in section 2.2.3, in the high scan rate regime, the dimensionless current tends to $(1 - \Theta)\Psi_p(\Lambda,\alpha)$ for model A and $(1 - \Theta_R)\Psi_p(\Lambda,\alpha)$ in the case of model B$_1$, the latter limit being correct. Thus, at high electrode coverage, where there is a relatively large difference between Θ and Θ_R, we anticipate a breakdown of model A as the scan rate increases. This is evident in Figure 9d ($\Theta = 0.5$), in which at low scan rates model A agrees well with the experimental data but tends to a significantly lower limit as we increase the voltage sweep rate.
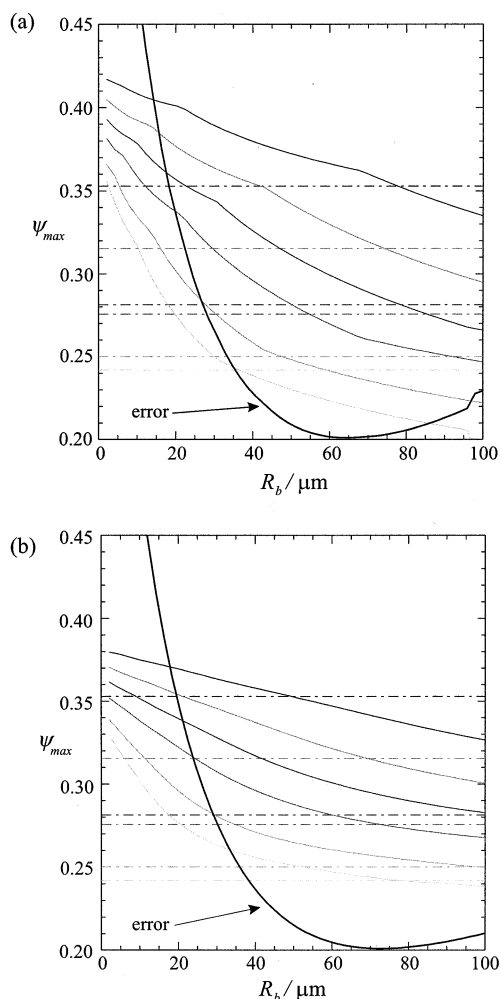

(a)

(b)

Figure 8. Results for the oxidation of 1.45 mM TMPD in 0.1 M TBAP/MeCN at the $\Theta = 0.5$ fabricated model gold electrode: simulations of the variation in the theoretically predicted value of ψ_{max} with block radius, R_b, for scan rates of (top to bottom) 0.02, 0.05, 0.1, 0.2, 0.5, and 1.0 V s^{-1} according to model (a) A and (b) B$_1$. The experimentally observed nondimensionalized currents are overlaid ($- \cdot -$). The curve labeled "error" is used to obtain R_b^{opt} and is referred to in the main text.

TABLE 1: Results for Experimental Data Fitting for Four 0.3 cm² Partially Blocked Gold Film Electrodes for Which the Distribution of Blocks Is Random

Θ	actual R_b (μm)	predicted R_b^{opt} (μm)	
		model A	model B
0.05	25		
0.15	40	41	40
0.25	50	43	41
0.50	75	65	74

In summary, at low scan rates and electrode coverage greater than or equal to 0.15, both models A and B$_1$ are in good agreement with the experimental data. However, as we increase the scan rate and coverage, we observe the failure of model A, whereas B$_1$ remains solid. The reason for the success of B$_1$ over A is due to the inclusion of randomness in the distribution of blocks, allowing for the possibility of overlap. Model A, however, does not include the effects of block overlap so breaks down in the limit $\nu_{dl} \rightarrow \infty$.

4.2. Basal Plane Pyrolytic Graphite Electrodes Partially Blocked with Microdroplets of THPD. *4.2.1. Size and Distribution of THPD Microdroplets.* The size and distribution
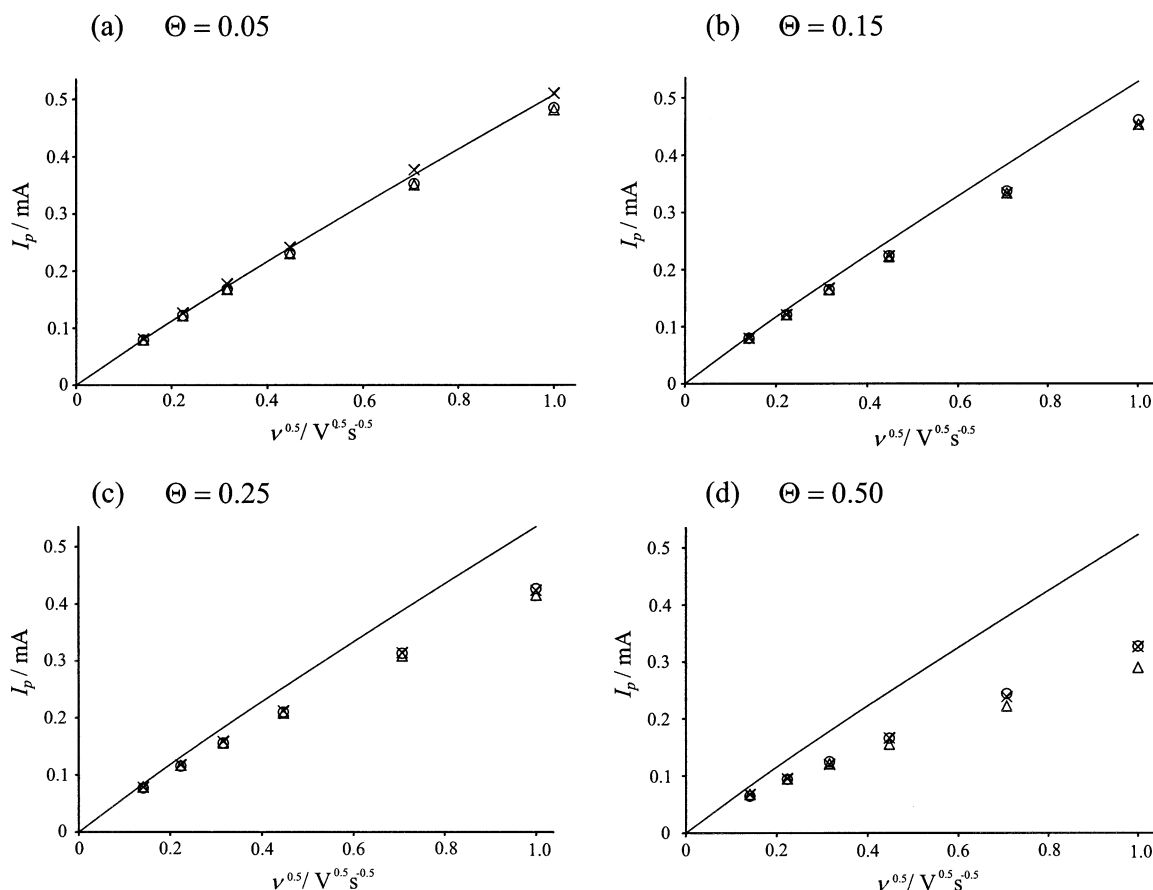
Figure 9. Results for the oxidation of 1.45 mM TMPD in 0.1 M TBAP/MeCN at the fabricated model gold electrodes: plots of theoretically predicted current (model A (△) and model B_1 (○)), experimentally observed current (×) and unblocked/theoretical maximum current vs the square root of the scan rate, where Θ = (a) 0.05, (b) 0.15, (c) 0.25, and (d) 0.5.

characteristics of THPD microdroplets immobilized on a bppg electrode has been reported in earlier work.[14g] In that work, visual inspection of the THPD microdroplets at two different values of THPD coverage was achieved by chemically nucleating metallic silver at the liquid|liquid interface;[14g] the deposition of 4 nmol of THPD on an area of 0.19 cm² of material produced droplets with mean radius size of 2 μm and standard deviation of 0.5 μm, while immobilization of 40 nmol of THPD gave values of 10.3 μm, standard deviation 3.3 μm. To confirm this, optical microscopy imaging (vide supra) of freshly cleaved bppg fragments immobilized with 20.3, 101.7, and 305.1 nmol of THPD was undertaken in air. Typical images are exhibited in Figure 10. Image size analysis of the microdroplets in at least two images at each THPD coverage yielded the following results. The analysis of 54 droplets for 20.3 nmol of THPD coverage resulted in mean radius values of 10.9 μm, standard deviation 8.4 μm; analysis of 44 droplets when 101.7 nmol of THPD was deposited on a bppg surface yielded mean radii of 10.7 μm, with a standard deviation of 5.7 μm; 27 droplets at 305.7 nmol of THPD gave the average radius of the droplets to be 18.2 μm, with 18.2 μm standard deviation. Although these results were obtained for nonimmersed microdroplets and may not reflect the true droplet sizes, we draw support for our data by their approximate agreement with the sizes reported in ref 14g. Although there is a large and significant spread in the data sets, suggesting that the assumption of monodispersed microdroplets in section 2 may not be applicable, it is noticeable that the mean radius values increase with increasing amount of THPD deposited.

4.2.2. Experiment vs Theory. Initial cyclic voltammograms were run in the scan rate range $0.02 \leq \nu \leq 2$ V s^{-1} on a bare 4.9 mm diameter bppg electrode so as to determine the experimental heterogeneous rate constant k_0 for the Co(III)/Co-(II) sepulchrate system and the diffusion coefficient of cobalt-(III) sepulchrate in aqueous 0.1 M sodium perchlorate. Values of $D = (6.7 \pm 0.2) \times 10^{-6}$ cm² s^{-1}, and $k_0 = (7.0 \pm 0.2) \times 10^{-3}$ cm s^{-1} were calculated. The value of k_0 agrees well with the value reported in the literature on platinum electrodes.[24,25] Modeling the CV data using DIGISIM 2.0[26] yielded an average value of the electron-transfer coefficient, α, of 0.58. Next the bppg electrode was treated with differing amounts of THPD using the method described in section 3, and cyclic voltammograms were recorded at scan rates of 0.02, 0.05, 0.1, and 0.2 V s^{-1}. Typical cyclic voltammograms are shown in Figure 11. It should be noted that the peak potential shifts to more positive potentials with increasing surface coverage, as expected.[10] This shift is *not* covered by the above theory, which deals solely with *currents* via eq 11. The peak current was determined from each voltammogram and then transformed into dimensionless form using eq 7. The results are shown in Figure 12. In general, the data show the trends expected from the theoretical work, decreasing with both block volume and increasing scan rate. At low block volumes, however, significant fluctuations in the dimensionless current occur. It is likely that these arise from an increased amount of edge plane surface in the basal plane electrode surface, exposed by the mechanical polishing of the bppg electrode on carborundum paper.[1a] This leads to nonlinear diffusion by virtue of the increased roughness of the electrode
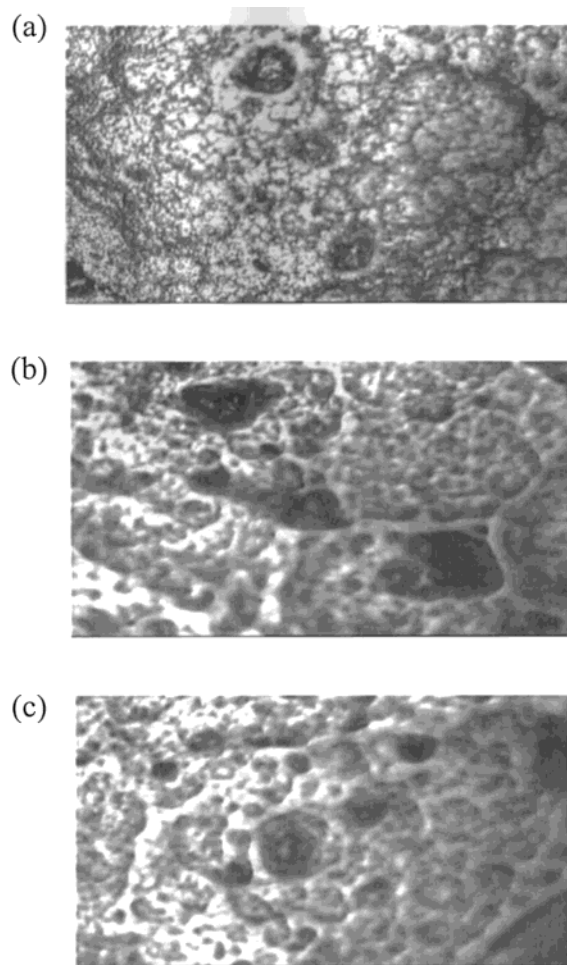
Figure 10. Optical images illustrating THPD microdroplets (seen as dark black globular features) immobilized on a basal plane pyrolytic graphite surface: (a) 20.3, (b) 101.7, and (c) 305.1 nmol of THPD. In each case, the abscissa is 445 μm, while the ordinate is 309 μm long.
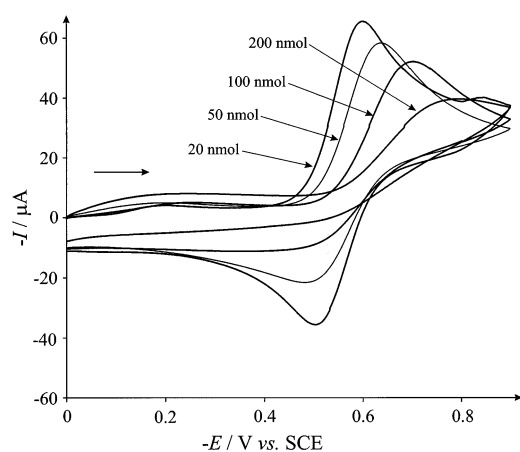

Figure 11. Cyclic voltammograms for the reduction of 1.65 mM cobalt(III) sepulchrate trichloride aqueous solutions containing 0.1 M sodium perchlorate at a 4.9 mm diameter basal plane pyrolytic graphite electrode modified with 20, 50, 100, and 200 nmol of THPD. The scan rate was 100 mV s^{-1}.

surface. Moreover, the density of microdroplets immobilized on such surfaces may vary across the surface,[1a] further contributing to the error.

Figure 13 illustrates the experimental and simulated data (for models A, B$_1$, and B$_2$) along with the "error" curve for the case of 100 nmol of THPD deposited on the electrode surface.
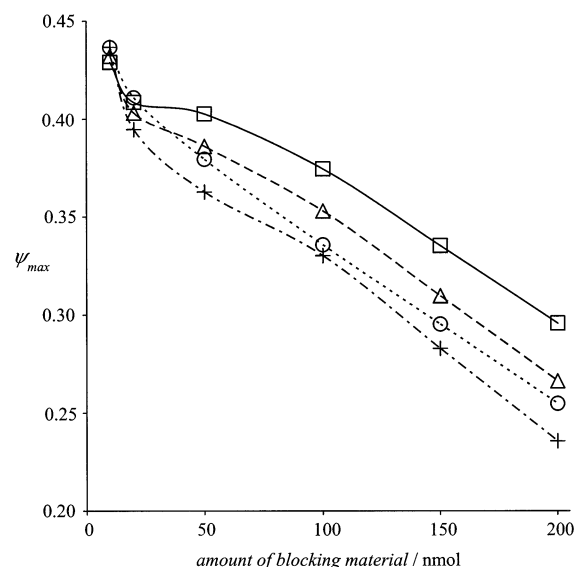

Figure 12. Variation of peak dimensionless reduction currents at a microdroplet-deposited bppg electrode with increasing volume of blocking material at scan rates of (○) 0.1, (△) 0.05, (□) 0.02, and (+) 0.2 V s^{-1}.

Optimized values of the droplet radius, R_b^{opt}, for a range of block volumes were obtained for each of the three models. Associated with every R_b^{opt} are values of Θ^{opt} and N_{hemi}^{opt}, given by eqs 27 and 28, respectively.

$$\Theta^{opt} = \frac{3V_{block}}{2R_b^{opt}A_{elec}} \tag{27}$$

$$N_{hemi}^{opt} = \frac{3V_{block}}{2\pi R_b^{opt\,3}} \tag{28}$$

The results for the fitting of R_b^{opt}, Θ^{opt} and N_{hemi}^{opt} in models A, B$_1$, and B$_2$ are given in Table 2. Note that for model B$_1$ there is an extra column, Θ_R^{opt} (obtained using eq 20), which is identical to the Θ^{opt} column for model B$_2$, as expected.

Figure 14 illustrates the variation of R_b^{opt} with block volume (given in moles) for all three models, along with the results from the imaging experiments. Both models A and B$_2$ predict an increase in droplet radius with block volume, the expected result, with model B$_2$ in better agreement with the experimental data. As forecast in section 2.3.2, model B$_1$ predicts a constant droplet radius of around 7.5 μm. The fact that model B$_1$ predicts a constant radius and B$_2$ is in good agreement with the actual data is very reassuring. *Our assumptions that we can treat the approximately hemispherical microdroplets on the electrode surface as disks of a single radius and that overlapping hemispheres retain their circular base appear to be viable.* Furthermore, at low coverage, models B$_1$ and B$_2$ predict the same droplet radius, as expected.

Figure 15 shows the variation in the global coverage, Θ^{opt}, with the block volume. As before, it can be seen that models B$_1$ and B$_2$ converge at low coverage. Model B$_1$ predicts a straight line through the origin. The gradient of this line is equal to 5.0 × 10^6 mol^{-1}, which is the value of 3RMM(THPD)/ $(2R_b^{opt}A_{elec}\rho(THPD))$ when R_b^{opt} is constant at 7.5 μm:

$$\Theta^{opt} = \frac{3V_{block}}{2R_b^{opt}A_{elec}} = \frac{3RMM(THPD)}{2R_b^{opt}A_{elec}\rho(THPD)}(\text{moles of material}) \tag{29}$$
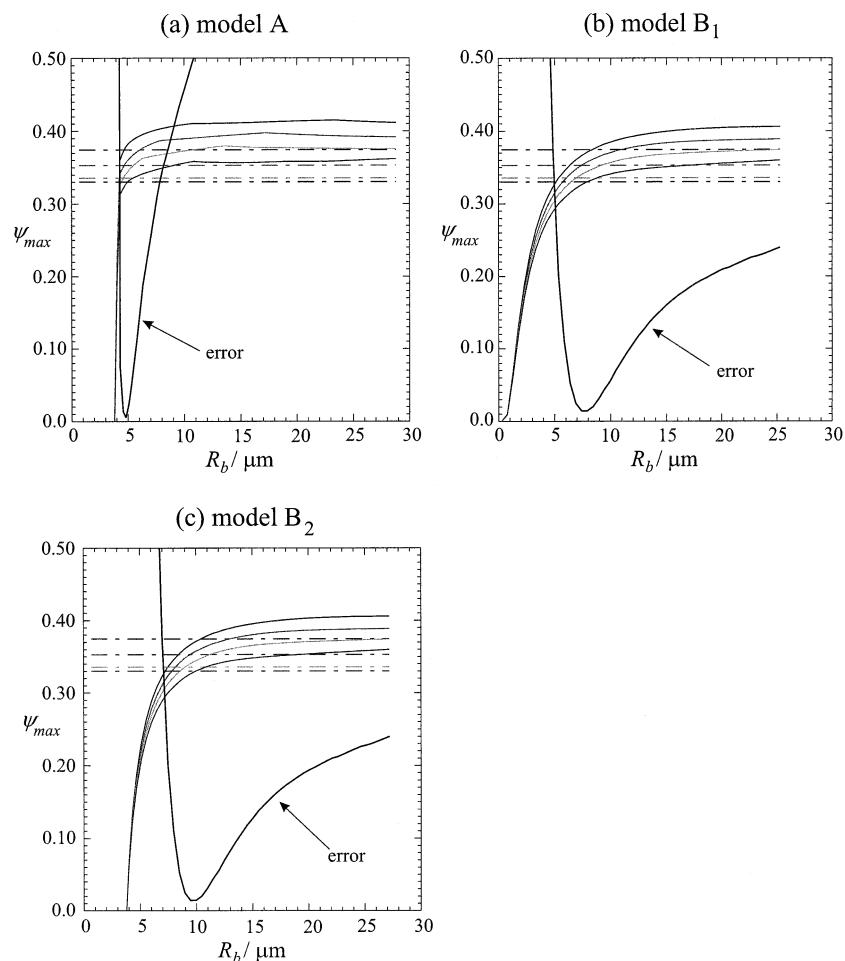
Figure 13. Reduction of cobalt(III) sepulchrate at the bppg electrode partially blocked with 100 nmol of THPD: simulations of the variation in the theoretically predicted value of ψ_{max} with block radius, R_b, for scan rates of (top to bottom) 0.02, 0.05, 0.1, and 0.2 V s^{-1} according to model (a) A, (b) B$_1$, and (c) B$_2$. The experimentally observed nondimensionalised currents are overlaid ($- \cdot -$). The curve labeled "error" is used to obtain R_b^{opt} and is referred to in the main text.

TABLE 2: Results from Experimental Data Fitting for a bppg Electrode of Size 0.19 cm^2 Partially Blocked with Microdroplets of THPD and Immersed into an Aqueous 0.1 M Sodium Perchlorate Solution Containing 1.65 mM Cobalt(III) Sepulchrate Trichloride

amount deposited (nmol)	model A			model B$_1$				model B$_2$		
	R_b^{opt} (μm)	Θ^{opt}	N_{block}^{opt}	R_b^{opt} (μm)	Θ^{opt}	Θ_R^{opt}	N_{block}^{opt}	R_b^{opt} (μm)	Θ^{opt}	N_{block}^{opt}
10										
20	3.0	0.25	1.7×10^5	6.5	0.12	0.11	1.7×10^4	6.5	0.12	1.7×10^4
50	3.4	0.56	2.9×10^5	6.9	0.28	0.24	3.5×10^4	7.8	0.24	2.4×10^4
100	4.8	0.79	2.1×10^5	7.7	0.49	0.39	5.0×10^4	9.8	0.39	2.4×10^4
150	6.4	0.89	1.3×10^5	7.5	0.76	0.53	8.1×10^4	10.1	0.53	2.8×10^4
200	8.3	0.91	8.0×10^4	7.6	1.0	0.63	1.0×10^5	12.1	0.63	2.6×10^4

In the above equation, RMM(THPD) refers to the relative molecular mass of THPD (444 g mol^{-1}) and ρ(THPD) is the density of the THPD liquid (0.93 g cm^{-3} at 293 K).[14g] The difference between models A and B$_2$ is also apparent in this figure. Model A predicts a global coverage that quickly tends to 1.0 as the block volume increases, whereas the corresponding increase in Θ^{opt} is much gentler for model B$_2$.

Finally, Figure 16 illustrates the dependence of N_{hemi}^{opt} on the block volume. Model B$_1$ predicts a straight line through the origin, the gradient of which is equal to 5.4×10^{11} mol^{-1}, as expected from eq 30, where R_b^{opt} is 7.5 μm:

$$N_{hemi}^{opt} = \frac{3V_{block}}{2\pi R_b^{opt\,3}} = \frac{3RMM(THPD)}{2\pi R_b^{opt\,3}\rho(THPD)}(\text{moles of material})$$

(30)

The difference between models A and B$_2$ is interesting. Model A predicts a general decrease in droplet density with increasing block volume. Although unlikely, a not impossible explanation is that during the growth stage large hemispheres engulf smaller ones hence reducing the number of droplets. In contrast, model B$_2$ predicts a constant droplet density. As we increase the block volume, we should increase the number of droplets. However, as suggested above, large hemispheres could engulf smaller ones thus reducing droplet density. If these two opposing effects were similar and cancel each other out, we would expect to see a constant droplet density—as predicted by model B$_2$.

In summary, model B$_2$ has the best agreement with the data obtained via imaging. Model B$_1$ is intriguing because it predicts the "building block" size of the droplets. In other words, according to model B$_1$, all THPD microdroplets present on a
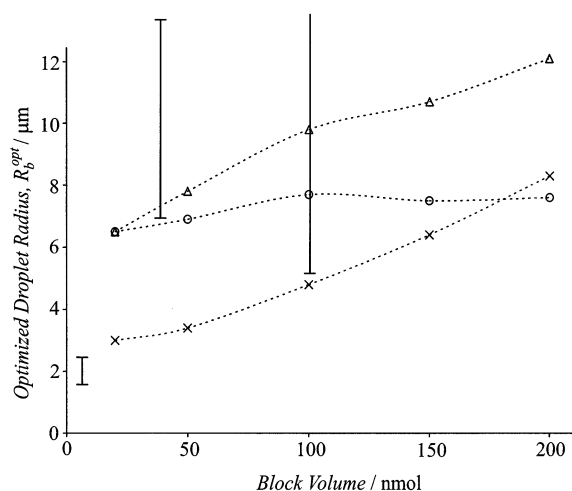
CV Response of Partially Blocked Electrodes. Part II

J. Phys. Chem. B, Vol. 107, No. 26, 2003 **6443**

Figure 14. Variation of optimized microdroplet radius (R_b^{opt}) with applied block substrate amount for models ($\times$) A, ($\bigcirc$) B$_1$, and ($\triangle$) B$_2$. Error bars indicate data from surface imaging.
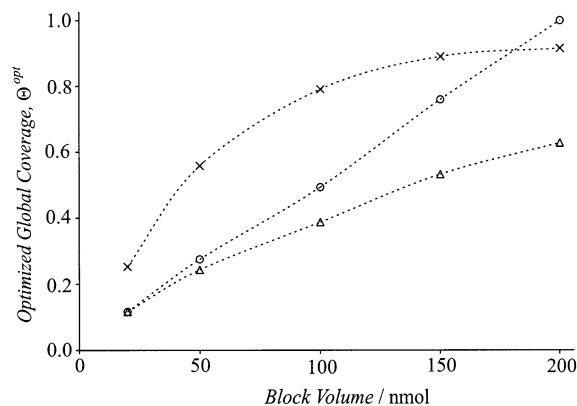

Figure 15. Variation of optimized global electrode coverage (Θ^{opt}) with applied blocked substrate amount for models ($\times$) A, ($\bigcirc$) B$_1$, and ($\triangle$) B$_2$.

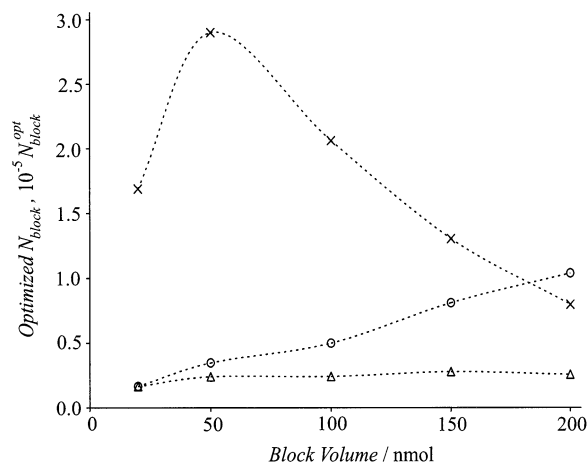**Figure 16.** Variation of optimized droplet number (N_{block}^{opt}) with applied blocked substrate amount for models ($\times$) A, ($\bigcirc$) B$_1$, and ($\triangle$) B$_2$.

bppg surface are made from droplets of radius $\sim$7.5 μm. The effect of disregarding overlap in the modeling is apparent in the differences between models A and B.

5. Conclusions

In this paper, we have seen how the principles developed in Part I for the simulation of electron transfer from a partially blocked electrode to solution phase species can be extended further to model heterogeneous electron-transfer processes at randomly distributed partially blocked electrodes. This has been evidenced via comparison of the simulation data with experimental PBEs, such as the idealized partially blocked gold film electrodes purposely constructed, and for electrodes modified with a random array of microdroplets. An interesting insight is the measured increase in droplet size as the total block volume increases, presumably to a limit. Such a limit is not observed in this work but would be attributed to a counterbalancing of surface tension (proportional to R^2) with edge tension (proportional to R). The further adaptation of the model presented to more complex electrochemical processes that are governed by blocking characteristics will be the subject of further investigation in our laboratories.

References and Notes

(1) (a) Murray, R. W. In *Electroanalytical Chemistry*; Bard, A. J., Ed.; Marcel Dekker: New York, 1984; Vol. 13, p 191. (b) Murray, R. W.; Ewing, A. G.; Durst, R. A. *Anal. Chem.* **1987**, *59*, 379A; (c) Murray, R. W. *Acc. Chem. Res.* **1980**, *13*, 135. (d) Murray, R. W. *Philos. Trans. R. Soc. London, Ser. A* **1981**, *302*, 253. (d) Murray, R. W., Ed. *Molecular Design of Electrode Surfaces*; John Wiley and Sons: New York, 1992. (e) Finklea, H. O. In *Encyclopædia of Analytical Chemistry*; Meyers, R. A., Ed.; John Wiley and Sons: Chichester, U.K., 2000; Vol. 11, p 10090.

(2) Laviron, E. In *Electroanalytical Chemistry*; Bard, A. J., Ed.; Marcel Dekker: New York, 1982; Vol. 12, p 53.

(3) Inzelt, G. In *Electroanalytical Chemistry*; Bard, A. J., Rubinstein, I., Eds.; Marcel Dekker: New York, 1994; Vol. 18, p 100.

(4) Scholz, F.; Meyer, B. In *Electroanalytical Chemistry*; Bard, A. J.; Rubinstein, I., Eds.; Marcel Dekker: New York, 1998; Vol. 20, p 1.

(5) Brookes, B. A.; Davies, T. J.; Fisher, A. C.; Evans, R. G.; Wilkins, S. J.; Yunus, K.; Wadhawan, J. D.; Compton, R. G. *J. Phys. Chem. B* **2003**, *107*, 1616.

(6) Baronas, R.; Ivanauskas, F.; Survila, A. *J. Math. Chem.* **2000**, *27*, 267.

(7) Survila, A.; Stasiukaitis, P. V.; Kanapeckaite, S.; Uksiene, V. *Chemija* **1998**, 143.

(8) Juozenas, A.; Sidlauskas, V.; Jurevicius, D. *Chemija* **1993**, 13.

(9) Caprani, A.; Deslouis, C.; Robin, S.; Tribollet, B. *J. Electroanal. Chem.* **1987**, *238*, 67.

(10) Amatore, C.; Savéant, J.-M.; Tessier, D. *J. Electroanal. Chem.* **1983**, *147*, 39 and references therein.

(11) Amatore, C.; Savéant, J.-M.; Tessier, D. *J. Electroanal. Chem.* **1983**, *146*, 37.

(12) (a) Dryfe, R. A. W.; Kralj, B. *Electrochem. Commun.* **1999**, *1*, 128. (b) Lillie, G. C.; Dryfe, R. A. W.; Holmes, S. M. *Analyst* **2001**, *126*, 1857. (c) Kralj, B.; Dryfe, R. A. W. *Phys. Chem. Chem. Phys.* **2001**, *3*, 3156. (d) Kralj, B.; Dryfe, R. A. W. *Phys. Chem. Chem. Phys.* **2001**, *3*, 5274. (e) Kralj, B.; Dryfe, R. A. W. *J. Phys. Chem. B* **2002**, *106*, 6732.

(13) Schmickler, W. *Interfacial Kinetics*; Oxford University Press: Oxford, U.K., 1996; pp 125−141.

(14) (a) Marken, F.; Webster, R. D.; Bull, S. D.; Davies, S. G. *J. Electroanal. Chem.* **1997**, *437*, 209. (b) Marken, F.; Blythe, A. N.; Wadhawan, J. D.; Compton, R. G.; Bull, S. D.; Davies, S. G. *J. Solid State Electrochem.* **2001**, *5*, 17. (c) Ball, J. C.; Marken, F.; Fulian, Q. L.; Wadhawan, J. D.; Blythe, A. N.; Schroeder, U.; Compton, R. G.; Bull, S. D.; Davies, S. G. *Electroanalysis* **2000**, *12*, 1017. (d) Wadhawan, J. D.; Compton, R. G.; Marken, F.; Bull, S. D.; Davies, S. G. *J. Solid State Electrochem.* **2001**, *5*, 301. (e) Wadhawan, J. D.; Schroeder, U.; Neudeck, A.; Wilkins, S. J.; Compton, R. G.; Marken, F.; Consorti, C. S.; de Souza, R. F.; Dupont, J. *J. Electroanal. Chem.* **2000**, *493*, 75. (f) Schroeder, U.; Wadhawan, J. D.; Evans, R. G.; Compton, R. G.; Wood, B.; Walton, D. J.; France, R. R.; Marken, F.; Page, P. C. B.; Hayman, C. M. *J. Phys. Chem. B* **2002**, *106*, 8697. (g) Wadhawan, J. D.; Evans, R. G.; Banks, C. E.; Wilkins, S. J.; France, R. R.; Oldham, N. J.; Fairbanks, A. J.; Wood, B.; Walton, D. J.; Schroeder, U.; Compton, R. G. *J. Phys. Chem. B* **2002**, *106*, 9619.

(15) Davies, T. J.; Banks, C. E.; Nuthakki, B.; Rusling, J. F.; France, R. R.; Wadhawan, J. D.; Compton, R. G. *Green Chem.* **2002**, *4*, 570.

(16) (a) Marken, F.; Compton, R. G. *Electrochim. Acta* **1998**, *43*, 2157. (b) Banks, C. E.; Rees, N. V.; Compton, R. G. *J. Phys. Chem. B* **2002**, *106*, 5810. (c) Wadhawan, J. D.; Marken, F.; Compton, R. G. *Pure Appl. Chem.* **2001**, *73*, 1947.

(17) Scharifker, B. *J. Electroanal. Chem.* **1988**, *240*, 61.

(18) In the case of an ensemble of electrodes, Reller and co-workers (Reller, H.; Kirowa-Eisner, E.; Gileadi, E. *J. Electroanal. Chem.* **1988**, *240*, 247) suggest that the current is largely independent of base shape unit. However, Scharifker's analytical work[17] shows that changing from cubic to hexagonal distributions generates a noticeable difference in the chronoamperometric current. This change is nevertheless small compared to the changes involved when a random electrode distribution is introduced.

(19) Chandrasekhar, S. *Rev. Mod. Phys.* **1943**, *15*, 1.

(20) Evans, U. R. *Trans. Faraday Soc.* **1945**, *41*, 365.

(21) Oldham, K. B.; Myland, J. C. *Electrochem. Commun.* **2001**, *2*, 541.

(22) (a) Avrami, M. *J. Chem. Phys.* **1939**, *7*, 1130. (b) Avrami, M. *J. Chem. Phys.* **1940**, *8*, 212. (c) Avrami, M. *J. Chem. Phys.* **1941**, *9*, 177.

(23) Nicholson, R. S. *Anal. Chem.* **1965**, *37*, 1351.

(24) Bond, A. M.; Lawrence, G. A.; Lay, P. A.; Sargeson, A. M. *Inorg. Chem.* **1983**, *22*, 2010.

(25) Creaser, I. I.; Harrowfield, J. M.; Herlt, A. J.; Sargeson, A. M.; Springborg, J.; Geue, R. J.; Snow, M. R. *J. Am. Chem. Soc.* **1977**, *99*, 3181.

(26) Rudolph. M.; Reddy, D. P.; Feldberg, S. W. *Anal. Chem.* **1994**, *66*, 589A.